



## Encoder-Only Image Registration

Xiang Chen<sup>a</sup>, Renjiu Hu<sup>b,c</sup>, Jinwei Zhang<sup>d</sup>, Yuxi Zhang<sup>a</sup>, Xinyao Yu<sup>e</sup>, Min Liu<sup>a</sup>, Yaonan Wang<sup>a</sup>, Hang Zhang<sup>f,\*</sup>

<sup>a</sup>School of Artificial Intelligence and Robotics, Hunan University, Changsha 410082, China

<sup>b</sup>Department of Radiology, Weill Medical College of Cornell University, New York, NY 10065, USA

<sup>c</sup>Sibley School of Mechanical and Aerospace Engineering, Cornell University, Ithaca, NY 14850, USA

<sup>d</sup>Department of Electrical and Computer Engineering, Johns Hopkins University, Baltimore, MD 21218, USA

<sup>e</sup>Department of Electrical and Computer Engineering, National University of Singapore, Singapore 117583

<sup>f</sup>Department of Electrical and Computer Engineering, Cornell University, Ithaca, NY 14850, USA

### ARTICLE INFO

#### Article history:

Received TBD

Received in final form TBD

\*Accepted TBD

Available online TBD

**Keywords:** Deformable image registration, Diffeomorphic transformation, Encoder-only Network, Large Deformation

### ABSTRACT

Learning-based techniques have significantly improved the accuracy and speed of deformable image registration. However, challenges such as reducing computational complexity and handling large deformations persist. To address these challenges, we analyze how convolutional neural networks (ConvNets) influence registration performance using the Horn-Schunck optical flow equation. Supported by prior studies and our empirical experiments, we observe that ConvNets play two key roles in registration: linearizing local intensities and harmonizing global contrast variations. Based on these insights, we propose the Encoder-Only Image Registration (EOIR) framework, designed to achieve a better accuracy-efficiency trade-off. EOIR separates feature learning from flow estimation, employing only a 3-layer ConvNet for feature extraction and a set of 3-layer flow estimators to construct a Laplacian feature pyramid, progressively composing diffeomorphic deformations under a large-deformation model. Results on five datasets across different modalities and anatomical regions demonstrate EOIR's effectiveness, achieving superior accuracy-efficiency and accuracy-smoothness trade-offs. With comparable accuracy, EOIR provides better efficiency and smoothness, and vice versa. The source code of EOIR will be publicly available on Github.

© 2025 Elsevier B. V. All rights reserved.

## 1. Introduction

Image registration, which establishes pixel/voxel correspondences between a pair of images and predicts a deformation field for their spatial alignment, is fundamental to medical imaging and computer vision Chen et al. (2021a). Essential for applications such as medical image segmentation Avants et al. (2008), motion tracking Fechter and Baltas (2020), surgical guidance Su et al. (2009), and diagnostic analysis Chen et al. (2013), pre-

cise image registration facilitates accurate disease detection and monitoring, and supports the progress of therapeutic procedures.

Traditional methods Ashburner (2007); Vercauteren et al. (2009) typically adopt variants of the Horn-Schunck (H-S) style variational formulation, involving a global dense displacement formulation and computationally expensive iterative processes. Recent advances in convolutional neural networks (ConvNets) Ronneberger et al. (2015) and transformers Dosovitskiy et al.; Liu et al. (2021) have enabled learning-based registration methods Balakrishnan et al. (2019); Hoopes et al. (2021) to achieve faster performance by amortizing optimization across cohorts, potentially improving accuracy when trained semi-supervised with label supervision. Despite progress, two major challenges

\*Corresponding author.

*e-mail:* [hz459@cornell.edu](mailto:hz459@cornell.edu) (Hang Zhang)

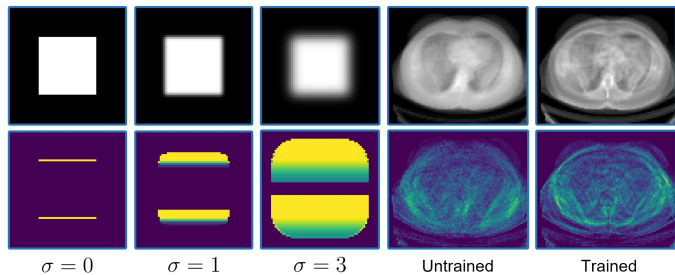


**Fig. 1. Visual demonstration of local intensity linearization.** The top row shows synthetic and real-world images, while the bottom row presents corresponding heatmaps (values 0 to 1) in the ‘viridis’ color map, where brighter areas indicate better linearization (heatmap generation detailed in the appendix). The first three columns show synthetic examples: a binary square (value 0 and 1) and its Gaussian-blurred versions with  $\sigma = 1$  and  $\sigma = 3$ . The last two columns display abdominal CT examples, with heatmaps derived from feature maps of untrained and trained ConvNets. Both Gaussian filtering and trained neural networks enhance local intensity linearization.

remain for learning-based registration methods, as outlined below.

**Lowering Computational Complexity:** Registering volumetric medical images demands considerable computational resources. To improve registration accuracy, advanced neural network modules, such as transformers Dosovitskiy et al.; Liu et al. (2021) or large conv kernels Jia et al. (2022); Ding et al. (2022), have been proposed, but these modules come with further increased computational demands. Despite this, the challenge of reducing computational complexity has been largely overlooked in the literature, with only a few learning-based methods Wang and Zhang (2020); Jia et al. (2023, 2024); Yang et al. (2024) explicitly addressing the efficiency issue. Yet, these approaches often lower computational complexity at the cost of accuracy, failing to achieve a practical balance between accuracy and efficiency for volumetric image registration, which remains an open challenge.

**Handling Large Deformations:** To manage large deformations, many existing approaches employ cascaded network architectures Zhao et al. (2019a); Jia et al. (2021), multi-scale coarse-to-fine strategies Mok and Chung (2021); Meng et al. (2024), or image pyramid structures Zhang et al. (2024a); Wang et al. (2024). While effective, these methods often rely on complex architectures, complicating the training process and increasing computational demands. We argue that the inability to effectively integrate prior knowledge limits the capacity of current neural networks from being fully utilized.

Previous research has shown that incorporating prior knowledge can improve the accuracy-efficiency trade-off in both image segmentation Zhang et al. (2023); Kervadec et al. (2019); Hu et al. (2021) and image registration Wang and Zhang (2020); Jia et al. (2023); Chen et al. (2024), which motivates the design of our architecture. Building on this principle, we identify two key roles of ConvNets in image registration, based on our empirical observations and prior studies Islam et al. (2020a); Wang et al. (2023); Zhang et al. (2024a): 1) **linearizing local intensities**, ensuring intensity changes vary linearly with spa-

tial coordinates to aid displacement estimation in textureless regions. 2) **harmonizing global contrast variations**, minimizing intensity discrepancies of the same anatomical regions across different subjects or phases to facilitate alignment. These two roles help produce image features that satisfy the brightness constancy assumption in the Horn-Schunck (H-S) optical flow equation Horn and Schunck (1981) (hereafter referred to as the **H-S assumption**).

The first role can be empirically observed in Fig. 1. The left three columns illustrate that simple conv operations, such as Gaussian filtering, help linearize local intensities of a simple structure (a uniform square in this case), aiding displacement recovery in textureless regions (the inner areas of the square). The right two columns demonstrate that trained ConvNet filters achieve superior linearization compared to untrained ones on more complex real-world abdominal data, as evidenced by a wider distribution of linearized locations. This observation aligns with Islam et al. (2020a), which showed that ConvNets implicitly learn features as a function of spatial coordinates, with deeper layers improving the readout of larger distances. Fig. 1 was created based on the H-S assumption, which relates the intensity change between a pair of images at a given location to the product of the displacement and the local image gradient.

The second role is supported by Wang et al. (2023), which observed that Pearson’s correlation between feature maps of different modalities increases with network depth, indicating that deeper ConvNet layers generate features more invariant to input modality. Additionally, our prior work Zhang et al. (2024a) demonstrated that image features learned for registration tasks can benefit segmentation, creating mutual improvements for both tasks. Given that ConvNets can bridge differences between modalities and harmonize image intensities into more uniform features across regions (as in segmentation), handling monomodal registration tasks with milder contrast variations, such as those addressed in this work, may require fewer convolutional layers and be more computationally efficient. Based on these observations, we propose the **Linearization-Harmonization (L-H) assumption** as a design guideline for our registration network: linearizing local intensities and harmonizing global contrast variations constitute the core roles of ConvNets in deformable image registration.

The H-S assumption informs us about what features are beneficial for registration, while the L-H assumption explains when a neural network can produce such features. In light of these insights, we introduce the following modifications to existing networks to guide our architecture design: 1) Unlike traditional learning-based methods Balakrishnan et al. (2019); Mok and Chung (2021); Chen et al. (2022) that concatenate moving and fixed images at the network input and process the entire network as a unified flow estimator, we extract feature maps from moving and fixed images independently. This separation of feature extraction from flow estimation enables the generation of image features consistent with the H-S assumption. 2) Because the H-S assumption holds primarily for small displacements, we implement a multi-level Laplacian with coarse-to-fine resolution. At each level, the moving image features are progressively warped using the deformation field from the preceding level, ensuring

that only residual deformations (ideally smaller than one voxel) need to be estimated at the current level. **3)** The network employs a single encoder with a few conv blocks. Features for each pyramid level are subsampled via trilinear interpolation from the encoder output. The pyramid architecture omits decoders and instead employs a set of flow estimators with one per pyramid level.

To accommodate these modifications, we propose the **Encoder-Only Image Registration (EOIR)** framework to address the aforementioned challenges (see Fig. 2 for an overview of the EOIR architecture). The name EOIR reflects the framework’s simplicity, as it utilizes only an encoder, foregoing a more complex encoder-decoder structure. While such terms may vary across contexts, we emphasize this minimal design to highlight its efficiency. The major contributions of this work are summarized as follows:

- We introduce a novel image registration framework, EOIR, which integrates the proposed L-H assumption and the classical H-S assumption as prior knowledge to guide its architecture design.
- By incorporating these priors, EOIR maximizes network capacity while retaining architectural simplicity. This enables our method to substantially reduce computational complexity without compromising accuracy, or achieve higher accuracy at comparable complexity levels.
- Experiments on five datasets spanning different modalities and anatomical regions demonstrate EOIR’s efficiency and effectiveness. Notably, EOIR secured second place in the test phase of Learn2Reg LUMIR Challenge 2024 Chen et al. (2025) using a sub-1MB-parameter network trained in two days on nearly 4,000 subjects, achieving both high accuracy and smooth deformations.

## 2. Related Work

The proposed EOIR framework falls under the category of learning-based registration models. In this section, we first review classic learning-based registration methods, followed by computationally efficient registration techniques, and conclude with models designed to handle large deformations.

### 2.1. Learning-Based Image Registration

Deformable image registration (DIR) is traditionally formulated as an energy optimization problem where dissimilarity between moving  $\mathbf{I}_m$  and fixed  $\mathbf{I}_f$  images is quantified using a dissimilarity function  $s(\cdot)$ . To counteract the ill-posed nature of DIR, a regularization term  $r(\cdot)$  constrains the deformation field. While traditional methods directly optimize the deformation field through gradient descent Avants et al. (2008) or discrete optimization Heinrich et al. (2013), learning-based approaches optimize the expected loss function to derive neural network weights  $\theta$  from a collection of image pairs  $D$ , as formulated below:

$$\hat{\theta} = \arg \min_{\theta} \{\mathbb{E}_{(\mathbf{I}_f, \mathbf{I}_m) \sim D} [\mathcal{L}(\mathbf{I}_f, \mathbf{I}_m, g_{\theta}(\mathbf{I}_f, \mathbf{I}_m))]\}. \quad (1)$$

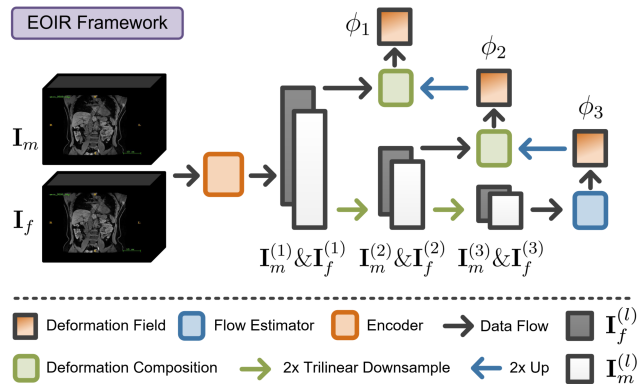


**Fig. 2. Visual illustration of the high-level EOIR framework using a three-level feature pyramid. Details of the encoder, flow estimators, deformation composition, and overall framework are provided in §3.4.**

In this equation,  $\mathcal{L}(\mathbf{I}_f, \mathbf{I}_m, \mathbf{u}) = s(\mathbf{I}_f, \mathbf{I}_m \circ \phi) + r(\mathbf{u})$  denotes the loss function. Here,  $\mathbf{I}_m \circ \phi$  represents the warping of the moving image by the deformation field  $\phi = \mathbf{I}_d + \mathbf{u}$ , where  $\mathbf{I}_d$  is the identity transformation grid. The functions  $s(\cdot)$  and  $r(\cdot)$  are the dissimilarity and regularization functions, respectively. Once the network is trained, the deformation field can be derived from  $\mathbf{u} = g_{\theta}(\mathbf{I}_f, \mathbf{I}_m)$  in a single forward pass.

Using Eq. (1) for unsupervised learning is much faster than traditional energy optimization methods and may benefit from label supervision such as segmentation loss, which may further increase the accuracy of anatomical alignment. VoxelMorph Balakrishnan et al. (2019), a pioneering learning-based model, entangles feature extraction and flow estimation in a single U-Net architecture Ronneberger et al. (2015), processing volumetric brain MR images in seconds. Following VoxelMorph, Dalca et al. (2019) introduces scaling and squaring layers Ashburner (2007) to ensure diffeomorphism. Vision transformers Liu et al. (2021) have also been incorporated into frameworks like TransMorph Chen et al. (2022), XMorpher Shi et al. (2022), NICE-Tans Meng et al. (2023), and H-ViT Ghahremani et al. (2024). Symmetric registration networks Mok and Chung (2020a), multi-channel architectures Chen et al. (2021b), dual-stream networks Kang et al. (2022), large-kernel convolutions Jia et al. (2022); Chen et al. (2024), and cascaded networks Zhao et al. (2019a); Mok and Chung (2021); Zhang et al. (2024a) further contribute to progress in the field. However, these improvements often lead to an exponential increase in parameters, raising computational demands, which can be challenging in resource-constrained clinical settings such as limited GPU memory or large volumetric datasets Liu et al. (2024).

### 2.2. Computationally-Efficient Image Registration

While the methods in §2.1 have improved registration accuracy, their high computational demands often hinder broader applicability. To date, only a few studies explicitly focus on efficiency Wang and Zhang (2020); Jia et al. (2023, 2024); Yang et al. (2024); Zhang et al. (2025b), though some achieve it through architectural design Balakrishnan et al. (2019); Chen et al. (2024); Zhang et al. (2024b). These pioneering efforts inspired EOIR’s design, demonstrating how integrating prior

knowledge can reduce complexity while maintaining accuracy, or even improve it.

DeepFlash Wang and Zhang (2020) approximates the original displacement space using a low-dimensional, band-limited space, performing neural network inference within this constrained domain. This accelerates training and inference without sacrificing accuracy compared to VoxelMorph, based on the assumption that flow fields inherently lack high frequencies in the Fourier domain. Similarly, FourierNet Jia *et al.* (2023) builds on this prior but improves efficiency by employing a model-driven decoder to better leverage the band-limited approximation, achieving a superior accuracy-efficiency trade-off. ShiftMorph Yang *et al.* (2024) skips the Fourier transform but applies a similar concept, operating at lower spatial resolutions for greater efficiency. LessNet Jia *et al.* (2024) eliminates the encoder entirely, significantly reducing network parameters while maintaining accuracy comparable to VoxelMorph Balakrishnan *et al.* (2019) and TransMorph Chen *et al.* (2022).

Additionally, some models incorporate other forms of prior knowledge to further improve efficiency. TextSCF Chen *et al.* (2024) uses a large visual-language model to enhance inter-regional anatomical understanding, outperforming models without priors in both efficiency and accuracy Balakrishnan *et al.* (2019); Chen *et al.* (2022); Mok and Chung (2021); Jia *et al.* (2022). The Slicer Network Zhang *et al.* (2024b), though designed for general medical image analysis, employs edge-preserving adaptive filters to expand the effective receptive field Luo *et al.* (2016), leading to better accuracy-efficiency trade-offs. Our EOIR framework integrates both the H-S and L-H assumptions, achieving an overall better accuracy-efficiency balance.

### 2.3. Large-Deformation Image Registration

Most learning-based models discussed in §2.1 and §2.2 exhibit limited performance on datasets involving large deformations. Even methods employing vision transformers or large convolutional kernels to expand the effective receptive field often fail to address such deformations adequately. To overcome this limitation, two primary architectural strategies have emerged: (1) recursive or cascaded flow estimators Zhao *et al.* (2019b); Jia *et al.* (2021); Zhang *et al.* (2025a), and (2) coarse-to-fine image pyramids Mok and Chung (2021); Zhang *et al.* (2024a); Meng *et al.* (2024).

The first approach, exemplified by VTN Zhao *et al.* (2019b) and VR-Net Jia *et al.* (2021), employs cascaded sub-networks that iteratively refine deformations through sequential steps, with each step generating a full-resolution deformation field. The second strategy, adopted in LapIRN Mok and Chung (2020a), IIRP-Net Ma *et al.* (2024), MemWarp Zhang *et al.* (2024a), and RDP Wang *et al.* (2024) progressively refines deformation fields using a coarse-to-fine pyramid framework, which often achieves better efficiency and large-deformation handling. CorrMLP Meng *et al.* (2024) further enhances this paradigm by integrating a correlation-aware multi-window MLP block into its coarse-to-fine architecture.

However, these methods typically lack explicit prior knowledge, requiring additional computational resources to process cascaded sub-networks or multi-scale features. In contrast, our

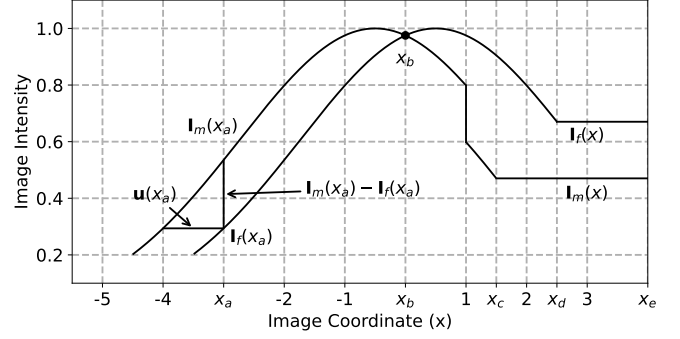


**Fig. 3.** A one-dimensional analogue of Equation (2) holds at  $x_a$ , where  $\frac{\mathbf{I}_m(x_a) - \mathbf{I}_f(x_a)}{u(x_a)} \approx \frac{d\mathbf{I}_f}{dx}(x_a)$ . Here,  $\mathbf{I}_m(x)$  is generated by translating  $\mathbf{I}_f(x)$  horizontally by  $-1$  and adding a global bias of  $-0.2$  for  $x > 1$ . However, the displacement cannot be determined at  $x_b$  (where  $\mathbf{I}_m(x_b) - \mathbf{I}_f(x_b) \approx 0$ ), between  $x = 2$  and  $x_d$  (where a global bias is applied), or between  $x_d$  and  $x_e$  (where  $\|\nabla \mathbf{I}_f\| = \|\nabla \mathbf{I}_m\| = 0$ ). Additional constraints are required to propagate displacements from surrounding regions.

EOIR framework adopts a coarse-to-fine strategy but achieves comparable registration accuracy with substantially improved efficiency, enabled by integrating the H-S and L-H assumptions as architectural priors.

## 3. Methodology

In this section, we begin by reviewing the Horn-Schunck (H-S) optical flow equation and explain how neural networks operating under the L-H assumption facilitate the production of image features that satisfy the H-S assumption. We then introduce the large-deformation diffeomorphic model, followed by a detailed description of our EOIR framework, including its network architecture and loss functions.

### 3.1. Horn-Schunck (H-S) Equation

The original H-S equation Horn and Schunck (1981) relates the displacement field  $\mathbf{u}(p)$  between images  $\mathbf{I}_m$  and  $\mathbf{I}_f$  to their intensity difference and gradient under sufficient spatial sampling:

$$\nabla \mathbf{I}_f(p) \cdot \mathbf{u}(p) = \mathbf{I}_m(p) - \mathbf{I}_f(p), \quad (2)$$

where  $\nabla \mathbf{I}_f(p) = \left[ \frac{\partial \mathbf{I}_f}{\partial x}, \frac{\partial \mathbf{I}_f}{\partial y}, \frac{\partial \mathbf{I}_f}{\partial z} \right]_p$  is the spatial gradient at voxel  $p \in \Omega$ . Equation (2) holds when  $\|\mathbf{u}(p)\|^2 < 1$  voxel, achievable through sufficient spatial downsampling (see  $x_a$  in Figure 3). To satisfy this small-displacement requirement, we adopt a Laplacian feature pyramid Mok and Chung (2021); Zhang *et al.* (2024a), where the number of pyramid levels  $n$  is determined by the maximum displacement  $d_{\max}$  in the dataset:

$$n > \log_2(d_{\max}) + 1, \quad (3)$$

ensuring deformations up to  $d_{\max}$  are resolved. The number of pyramid levels is determined by the maximum displacement in a given dataset. While adjusting the levels can reduce complexity, we adopt a 5-level pyramid for simplicity, which generalizes well across most datasets. See §4.4.3 for a comparison of the effects of varying pyramid levels across datasets.

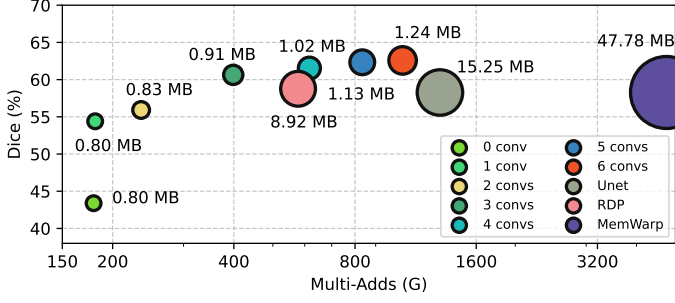


**Fig. 4.** Visual comparison of the trade-off between avg. Dice and computational complexity for varying numbers of conv layers in the EOIR encoder ( $n_c$  from 0 to 6), alongside top-performing pyramid methods RDP Wang et al. (2024) and MemWarp Zhang et al. (2024a) on the abdomen dataset. Circle size and labels indicate network parameter size, and multi-adds (G) are plotted on a logarithmic x-axis. (see appendix for further metric details)

Despite the use of a pyramid, Equation (2) may fail even with sub-voxel displacements in three scenarios: 1) at locations with insufficiently large image gradients, indicating flat or noisy regions where no local constraints can be imposed ( $x_d$  to  $x_e$  in Fig. 3); 2) when the intensity difference between the moving and fixed images at certain locations is close to zero ( $x_b$  in Fig. 3); 3) when a global intensity bias is added to the moving or fixed image, as between  $x = 2$  and  $x_d$  in Fig. 3). Voxels in these scenarios can be addressed by feature linearization via a neural network and global smoothness constraints through a loss function. The former offers features with local intensity linearization, while the latter can assist in propagating displacements from surrounding valid locations.

### 3.2. Large-Deformation Diffeomorphic Model

For large diffeomorphic deformations, a widely used approach Arsigny et al. (2006); Ashburner (2007) involves utilizing a stationary velocity field (SVF)  $\mathbf{v}$ . This field is integrated over unit time from  $t = 0$  to  $t = 1$  to produce the final deformation field  $\phi^{(1)}$ , starting from the identity transformation  $\phi^{(0)} = \mathbf{I}_d$ . The integration is governed by the following ordinary differential equation (ODE):

$$\frac{d\phi^{(t)}}{dt} = \mathbf{v}(\phi^{(t)}). \quad (4)$$

However, as noted in Section §3.1, modeling displacements up to a maximum  $d_{max}$  requires a Laplacian feature pyramid of  $n$  levels to ensure  $2^{n-1} > d_{max}$  (Equation 3). Given that  $n$  residual deformation fields are estimated at each pyramid level and must be composed to form the final deformation field, a single SVF is insufficient to adequately model the dynamics across different pyramid levels. Therefore, we utilize  $n$  SVFs, each corresponding to a different pyramid level, to govern the evolution of the deformation. Consequently, with  $\mathbf{v}^{(t)}$  as a piecewise constant function representing the velocity field at time  $t$ , the deformation evolves as the following ODE:

$$\frac{d\phi^{(t)}}{dt} = \mathbf{v}^{(t)}(\phi^{(t)}). \quad (5)$$

The integration of Equation (5) can be discretized into a finite number of steps, expressed as:

$$\phi^{(t+\Delta t)} = (\mathbf{I}_d + \Delta t \mathbf{v}^{(t)}) \circ \phi^{(t)}, \quad (6)$$

where  $\Delta t$  is the integration step size. This method models large deformations as a sequence of small deformations at each step. To ensure accurate approximation, the step number must be large enough to capture each deformation sufficiently.

### 3.3. Integration and Deformation Field Composition

In learning-based registration models such as VoxelMorph, which output a single deformation field for an image pair, Equation (4) can parametrize the deformation field. The *scaling and squaring* method, derived from Lie Theory by Arsigny et al. (2006), is an efficient integration solution. It's widely used for rapid integration in learning-based registration models Dalca et al. (2019); Mok and Chung (2021), enabling efficient computation of diffeomorphic deformations.

Models using a feature pyramid, which must compose multiple deformation fields from coarse to fine, require more careful handling of integration and composition. For example, LapIRN Mok and Chung (2021) and MemWarp Zhang et al. (2024a) use a Laplacian feature pyramid and compose deformation fields across levels by addition. While computationally less demanding, this approach can result in a poorer trade-off between deformation smoothness and registration accuracy Chen et al. (2024), as well as slower convergence and a tendency to settle at sub-optimal local minima Vercauteren et al. (2009).

To address this issue, we propose discretizing the unit time into a substantial number of smaller intervals, specifically  $n \times m$  steps, where  $n$  is the number of pyramid levels, and  $m$  is the number of steps within each level corresponding to the pyramid hierarchy. Let  $\phi^{ij}$  denote the  $j^{\text{th}}$  step of the  $i^{\text{th}}$  level, the final deformation field  $\phi$  can be approximated as:

$$\begin{aligned} \phi &\approx \phi^{111} \circ \phi^{112} \circ \dots \circ \phi^{11m} \circ \\ &\quad \phi^{211} \circ \phi^{212} \circ \dots \circ \phi^{21m} \circ \\ &\quad \dots \\ &\quad \phi^{n11} \circ \phi^{n12} \circ \dots \circ \phi^{n1m}. \end{aligned} \quad (7)$$

While naively computing Equation (7) demands  $\mathcal{O}(nm)$  complexity and may prove computationally burdensome, employing the *scaling and squaring* method by Arsigny et al. (2006) for each level significantly reduces this to  $\mathcal{O}(n \log m)$ .

### 3.4. Neural Network Architecture

The design of the EOIR architecture is guided by the H-S and L-H assumptions. It is composed of three main components: an encoder for feature extraction, a set of flow estimators, and a deformation field composition module. In the following sections, we will detail each component and conclude with a discussion of the loss function for deep supervision Lee et al. (2015).

#### 3.4.1. Encoder

Based on the H-S assumption, we construct a multi-level Laplacian feature pyramid (Fig. 2). To model large-deformation diffeomorphic transformations, we approximate the final deformation field via integration over small intervals using Equation (7), where  $n$  pyramid levels each contain  $m$  intervals. Each interval within a pyramid level follows the small-deformation

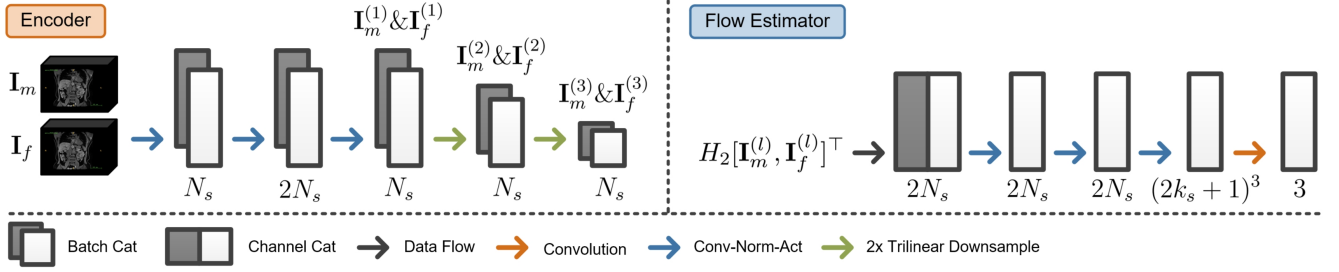


**Fig. 5. Visual illustration of the components of the encoder and flow estimator in EOIR.** To illustrate the encoder structure, we use a three-level feature pyramid, which consists of three Conv-Norm-Act blocks and two trilinear downsampling layers, producing three pairs of moving and fixed images at different scales. Each pyramid level’s flow estimator shares the same structure but with different weights; it consists of a Hadamard transformation, three Conv-Norm-Act blocks, and a single convolution to produce a residual displacement field at that level. In our experiments, we empirically set  $K_s = 1$ .

model  $\phi(p) = p + \mathbf{u}(p)$ . Despite these design choices, Fig. 3 illustrates scenarios where displacement determination remains ambiguous, even under sufficient downsampling (with  $\|\mathbf{u}(p)\|^2 < 1$  voxel), due to vanishing gradients or contrast variations.

The proposed L-H assumption, grounded in empirical observations from both synthetic and clinical data (Fig. 1) and prior research Islam et al. (2020b); Wang et al. (2023); Zhang et al. (2024a), explains that trained ConvNets for image feature extraction can effectively linearize and harmonize local intensities in mono-modal registration tasks. Additionally, Fig. 1 demonstrates a considerable increase in the number and distribution of valid locations satisfying the H-S assumption when using trained ConvNets.

Guided by the H-S and L-H assumptions and the small-deformation model for each interval, we propose that local intensity linearization within small voxel neighborhoods is sufficient to recover large diffeomorphic deformations. Thus, we employ only three learnable convolutional layers, rather than a complex encoder-decoder U-Net Ronneberger et al. (2015), to efficiently act as local intensity linearizers and contrast harmonizers, achieving an optimal accuracy-efficiency trade-off. While additional layers ( $n_c > 3$ ) could improve registration accuracy, the marginal gains diminish rapidly beyond three layers (see Fig. 4).

The encoder comprises three Conv-Norm-Act blocks, each containing a learnable  $3 \times 3 \times 3$  convolutional layer, instance normalization Ulyanov (2016), and a ReLU activation. As shown in Figure 5 (left), the encoder begins with  $N_s$  channels, expands to  $2N_s$  via an inverted bottleneck design Sandler et al. (2018), and contracts back to  $N_s$ . Combined with  $n - 1$  rounds of  $2 \times$  spatial downsampling, this design ensures effective local intensity linearization and contrast harmonization.

### 3.4.2. Flow Estimator

With the locally linearized and harmonized feature maps from the encoder, we apply  $2 \times$  trilinear downsampling to the feature maps  $n - 1$  times, resulting in an  $n$ -level feature pyramid. This pyramid is structured to handle displacements with a maximum of  $d_{max} < 2^{n-1}$  (Equation 3). At each pyramid level, a flow estimator, consisting of a Hadamard transform layer Pratt et al. (1969) and several conv blocks, generates the residual flow. The flow estimator’s structure is depicted in the right panel of Fig. 5 and further detailed below.

The ODE (2) shows that displacements are linked to the inten-

sity differences between the moving and fixed images. Rather than using neural network to learn this difference, we explicitly apply a Hadamard transform to the feature maps:

$$H_2[\mathbf{I}_m^{(l)}, \mathbf{I}_f^{(l)}]^\top = [\mathbf{I}_m^{(l)} + \mathbf{I}_f^{(l)}, \mathbf{I}_m^{(l)} - \mathbf{I}_f^{(l)}]^\top, \quad (8)$$

where  $\mathbf{I}_m^{(l)}$  and  $\mathbf{I}_f^{(l)}$  are the moving and fixed image feature maps at pyramid level  $l$ , and  $H_2 = \begin{bmatrix} 1 & 1 \\ 1 & -1 \end{bmatrix}$ . After the transform, the moving and fixed features are stacked along the channel dimension, processed with three Conv-Norm-Act blocks, and a linear layer on each voxel produces final displacement fields.

### 3.4.3. Deformation Field Composition

We represent the velocity field at time  $t$  by a piece-wise constant function,  $\mathbf{v}^{(l)}$ , where the number of pieces corresponds to the number of feature pyramid levels  $n$ . This yields multiple stationary ODEs (5) across different periods within the unit time. Additionally, under the H-S assumption that the displacement difference between adjacent periods is minimal, we can employ Equation (8) to approximate the deformation composition process throughout our feature pyramid, thereby promoting a diffeomorphic transformation.

As illustrated in Fig. 6, the deformation field composition at the  $l^{th}$  level of the pyramid involves the following steps. Starting with feature maps  $\mathbf{I}_m^{(l)}$  and  $\mathbf{I}_f^{(l)}$ , and the deformation field  $\phi_{l+1}$  from the previous level:

$$\begin{aligned} \tilde{\phi}_{l+1} &= \text{up}(\phi_{l+1}), \\ \mathbf{u}_l &= f_e^{(l)}(\mathbf{I}_m^{(l)} \circ \tilde{\phi}_{l+1}, \mathbf{I}_f^{(l)}), \\ \Delta\phi_l &= \exp(\mathbf{u}_l), \\ \phi_l &= \tilde{\phi}_{l+1} \circ \Delta\phi_l, \end{aligned} \quad (9)$$

where  $\text{up}(\cdot)$  denotes  $2 \times$  trilinear upsampling and scaling,  $\exp(\cdot)$  refers to the scaling and squaring function applied to the displacement field, and  $\circ$  denotes the warping function. The  $\mathbf{u}_l$  represents the residual displacement field at level  $l$ , and  $f_e^{(l)}(\cdot, \cdot)$  is the flow estimator at level  $l$ .

### 3.4.4. Overall Framework & Deep Supervision

With the encoder, flow estimator, and deformation field composition components in place, we have constructed the EOIR

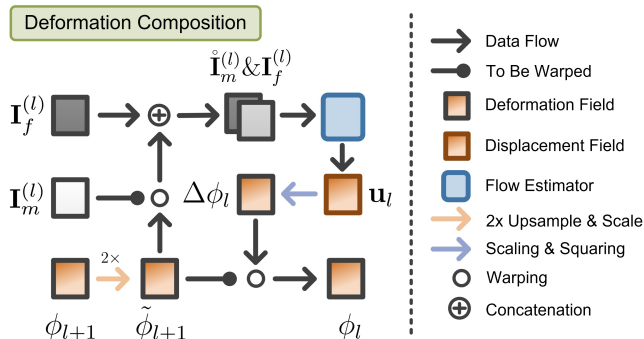


Fig. 6. Visual illustration of the deformation composition process, with corresponding equation derivations in §3.4.3.

framework. This framework is visually illustrated in Fig. 2 using a 3-level pyramid. To optimize the network weights, we employ deep supervision Lee et al. (2015), which applies a loss function at each level of the pyramid. The total loss is calculated as an exponentially decayed weighted sum across all levels:

$$\mathcal{L} = \sum_{l=1}^n \frac{1}{2^{l-1}} \left[ s(d(\mathbf{I}_m, l) \circ \phi_l, d(\mathbf{I}_f, l)) + \lambda r(\mathbf{u}_l) \right]. \quad (10)$$

Here,  $n$  represents the number of pyramid levels,  $s(\cdot, \cdot)$  denotes the dissimilarity function,  $d(\cdot, l)$  downsamples the input image by a factor of  $2^{l-1}$ , and  $r(\cdot)$  represents the smoothness regularization function applied to the displacement field  $\mathbf{u}_l$  before scaling and squaring. We use  $r(\mathbf{u}_l) = \|\nabla \mathbf{u}_l\|^2$  as the regularization function, with  $\lambda$  as its coefficient.

## 4. Experiments & Results

In this section, we evaluate the proposed EOIR against state-of-the-art image registration methods across five datasets, covering various imaging modalities, input constraints, and anatomies. The following subsections detail the datasets, implementation details, baseline methods, and evaluation metrics. We then present qualitative and quantitative results, including analyses of accuracy-efficiency trade-offs, accuracy-smoothness comparisons, and an ablation study. The source code of EOIR will be publicly available on Github.

### 4.1. Datasets

The datasets span both CT and MRI modalities, with inter-subject and intra-subject settings, as well as unsupervised and semi-supervised configurations that include segmentation masks. In summary, we use the semi-supervised Abdomen CT dataset for inter-subject registration Xu et al. (2016), the semi-supervised OASIS dataset Marcus et al. (2007), the unsupervised large-scale LUMIR dataset Dufumier et al. (2022); Taha et al. (2023); Marcus et al. (2007) for inter-subject brain MR image registration, the ACDC dataset Bernard et al. (2018) for cardiac image registration, and the HippocampusMR Simpson et al. (2019) for Hippocampus MR image registration.

#### 4.1.1. Abdomen CT Dataset

Inter-subject organ registration on abdominal images is challenging due to the great variability and large deformations across subjects. We utilize a dataset of 30 abdominal CT scans Xu et al. (2016), each accompanied by segmentation masks for 13 anatomical structures. The dataset is divided into training, validation, and test sets, with 20, 3, and 7 scans, respectively, resulting in 380 ( $20 \times 19$ ) training pairs, 6 ( $3 \times 2$ ) validation pairs, and 42 ( $7 \times 6$ ) testing pairs. All images were resampled to a voxel resolution of 2 mm and standardized to a spatial size of  $192 \times 160 \times 256$ .

#### 4.1.2. ACDC Dataset

We also evaluate the proposed EOIR in intra-subject cardiac MR image registration using the ACDC dataset Bernard et al. (2018), which includes 80 subjects for training, 20 for validation, and 50 for testing. For each subject, the end-diastole (ED) and end-systole (ES) images have ground-truth segmentations for the left ventricle blood pool (LVBP), left ventricle myocardium (LVM), and right ventricle (RV). We perform registration from both ED to ES and ES to ED, resulting in 160 training pairs, 40 validation pairs, and 100 test pairs. All images are pre-processed to  $128 \times 128 \times 16$  (spacing:  $1.8 \times 1.8 \times 10 \text{mm}^3$ ) through resampling, normalization, cropping, and padding.

#### 4.1.3. OASIS Dataset

For semi-supervised inter-subject brain MR image registration, we use the OASIS dataset Marcus et al. (2007) from Task 3 of the Learn2Reg challenge 2021 Hering et al. (2022). The dataset consists of T1-weighted brain MRI scans from 414 subjects. We used 394 unpaired scans for training, with 19 image pairs from 20 scans for validation and leaderboard ranking<sup>1</sup>. In our experiments, we directly used the challenge-provided data, pre-processed with bias correction, skull stripping, alignment, and cropping to  $160 \times 192 \times 224$  dimensions.

#### 4.1.4. LUMIR Dataset

LUMIR Dufumier et al. (2022); Taha et al. (2023); Marcus et al. (2007) is designed for large-scale unsupervised brain MR image registration, part of Task 2 in the Learn2Reg challenge 2024. The dataset includes 3,384 subjects for training and 40 subjects for validation, with 10 training subjects manually annotated with landmarks by physicians, resulting in 38 validation pairs. All images are provided in NIfTI format, resampled, and cropped to the region of interest, with a final size of  $160 \times 224 \times 192$  and voxel spacing of  $1 \times 1 \times 1 \text{mm}^3$ .

#### 4.1.5. HippocampusMR Dataset

The HippocampusMR dataset Simpson et al. (2019) focuses on hippocampus MR image registration across subjects, including healthy adults and adults with non-affective psychotic disorders, as part of the Learn2Reg 2020 challenge. We split the dataset into training, validation, and testing sets with 200, 20, and 40 samples, respectively. All images are preprocessed to a

<sup>1</sup><https://learn2reg.grand-challenge.org/evaluation/task-3-validation/leaderboard/>

resolution of  $64 \times 64 \times 64$  voxels with a spacing of  $1 \times 1 \times 1$  mm<sup>3</sup>.

## 4.2. Implementation Details and Baseline Methods

### 4.2.1. Training Details

In this study, all models were developed using the PyTorch library in Python, executed on a system with an A100 GPU. The Adam optimizer was employed for training, with an initial learning rate of  $1e-4$  and a polynomial learning rate scheduler with a decay rate of 0.9. The channel parameters for EOIR’s encoder and flow estimator were set to  $N_s = 32$  and  $k_s = 1$ , unless otherwise specified. The number of image pyramid levels is set to  $n = 5$ , and the number of time steps in each period for Equation (8) is set to  $m = 7$ , unless otherwise specified. Dataset-specific details, including the dissimilarity function  $s(\cdot)$ , inclusion of Dice loss, and other training parameters, are provided in the appendix. For a fair comparison, all models were trained under identical conditions or, where necessary, using the optimal settings outlined in their original publications.

### 4.2.2. Baseline Methods

We compare our EOIR framework with several state-of-the-art non-iterative, learning-based baseline models, including VoxMorph Balakrishnan et al. (2019), TransMorph Chen et al. (2022), LKU-Net Jia et al. (2022), Fourier-Net Jia et al. (2023), RDP Wang et al. (2024), LapIRN Mok and Chung (2021), MemWarp Zhang et al. (2024a) and CorrMLP Meng et al. (2024). For the Abdomen CT dataset, we additionally include discrete optimization-based methods ConvexAdam Siebert et al. (2021) and SAMConvex Li et al. (2023) in the comparison, as these are highly effective for handling large deformations. For results on the OASIS and LUMIR datasets, we obtained evaluation scores from the public leaderboard or respective publications. In the case of the ACDC and Abdomen CT datasets, we used publicly available code for each model and fine-tuned them to achieve optimal performance.

### 4.2.3. Evaluation Metrics

Following established methodologies Dalca et al. (2018); Balakrishnan et al. (2019); Mok and Chung (2021); Chen et al. (2022) and challenge protocols Hering et al. (2022), we evaluate anatomical alignment using the Dice Similarity Coefficient (Dice) and the 95% Hausdorff Distance (HD95). Target registration error (TRE) is also computed if the dataset provide ground-truth landmark points. To assess field smoothness, we measure the standard deviation of the logarithm of the Jacobian determinant (SDlogJ), and non-diffeomorphic volumes (NDV) Liu et al. (2024). Additionally, computational complexity is assessed using the multiply-add operations (Multi-Adds, G) and total parameter size (Params, MB). The inference time on cardiac image registration and hippocampus image registration are also presented to demonstrate the efficiency of EOIR.

## 4.3. Results & Analysis on Registration Accuracy

### 4.3.1. Handling Large Deformations

We demonstrate the capability of handling large deformations using inter-subject abdominal CT registration. As shown in

Table 1 and Fig. 7, EOIR outperforms all other methods in registration accuracy without compromising smoothness. Specifically, EOIR surpasses the best conventional learning-based method, LKU-Net, by 14.87%, the best image pyramid-based method, MemWarp, by 0.65%, the best efficiency-driven method, FourierNet, by 41.66%, and the best discrete optimization-based method, SAMConvex, by 13.01%. It’s worth noting that while MemWarp matches EOIR in registration accuracy, it uses additive deformation composition, resulting in a less smooth field. Although FourierNet achieves a smoother field, it falls behind in registration accuracy. Both discrete optimization-based methods generate smooth deformation fields and improve upon efficiency-driven methods, but their registration accuracy lags behind all image pyramid-based methods and EOIR.

**Table 1. Quantitative comparison on the abdomen CT dataset. Best-performing metrics are in bold. Symbols indicate direction:  $\uparrow$  for higher is better,  $\downarrow$  for lower is better. “Initial” refers to baseline results before registration.**

Model	Dice (%) $\uparrow$	HD95 (mm) $\downarrow$	SDlogJ $\downarrow$
Initial	30.68	29.77	-
VoxelMorph Balakrishnan et al. (2018)	47.05	23.08	0.13
TransMorph Chen et al. (2022)	47.94	21.53	0.13
LKU-Net Jia et al. (2022)	52.78	20.56	0.98
LapIRN Mok and Chung (2020b)	54.55	20.52	1.73
CorrMLP Meng et al. (2024)	56.11	19.52	0.16
RDP Wang et al. (2024)	58.77	20.07	0.22
MemWarp Zhang et al. (2024a)	60.24	19.84	0.53
LessNet Jia et al. (2024)	42.03	27.03	<b>0.07</b>
FourierNet Jia et al. (2023)	42.80	22.95	0.13
ConvexAdam Siebert et al. (2021)	51.10	23.14	0.11
SAMConvex Li et al. (2023)	53.65	18.66	0.12
<b>EOIR (Ours)</b>	<b>60.63</b>	<b>17.61</b>	0.17

### 4.3.2. Handling Local Intra-subject Motions

Unlike inter-subject abdominal CT registration, intra-subject cardiac registration focuses on tracking local cardiac motion, such as the movement of the left and right ventricles, during the complete phases of the cardiac cycle. As shown in Table 2, EOIR outperforms all other methods in registration accuracy, measured by Dice score. Specifically, EOIR surpasses the best conventional learning-based method, LKU-Net, by 3.1%, the best image pyramid-based method, RDP, by 1.1%, and the best efficiency-driven method, FourierNet, by 3.0%. It is worth noting that LessNet and LapIRN are excluded from Table 2, as they cannot handle short-axis data, and no straightforward approach was found to enable them to do so.

**Table 2. Quantitative comparison on the cardiac ACDC dataset. Best-performing metrics are highlighted in bold. Symbols indicate direction:  $\uparrow$  for higher is better,  $\downarrow$  for lower is better. “Initial” refers to baseline results before registration. “MAs (G)” stands for multi-adds (G) and “PS (MB)” stands for parameter size (MB). “Time” is the average inference time for one registration pair. GM(MB) is the occupied GPU memory in the inference.**

Model	Dice (%) $\uparrow$	HD95 (mm) $\downarrow$	SDlogJ $\downarrow$	MAs (G) $\downarrow$	PS (MB) $\downarrow$	Time $\downarrow$	GM(MB) $\downarrow$
Initial	58.14	11.95	-	-	-	-	-
TransMorph Chen et al. (2022)	74.97	9.44	0.045	50.20	46.69	0.26	18.3
VoxelMorph Balakrishnan et al. (2018)	75.26	9.33	<b>0.044</b>	19.55	0.32	<b>0.18</b>	<b>2.7</b>
LKU-Net Jia et al. (2022)	76.53	9.13	0.049	160.50	33.35	0.22	3.9
Fourier-Net Jia et al. (2023)	76.61	9.25	0.047	86.07	17.43	0.27	3.1
CorrMLP Meng et al. (2024)	77.31	<b>9.00</b>	0.056	47.59	4.19	0.28	3.3
MemWarp Zhang et al. (2024a)	76.74	9.67	0.108	1270.00	47.78	0.58	12.7
RDP Wang et al. (2024)	78.06	9.02	0.076	154.00	8.92	0.36	4.1
EOIR ( $N_s = 8$ )	78.28	9.14	0.071	11.02	0.11	0.25	2.9
<b>EOIR (Ours)</b>	<b>78.91</b>	9.07	0.084	114.21	0.91	0.26	4.5

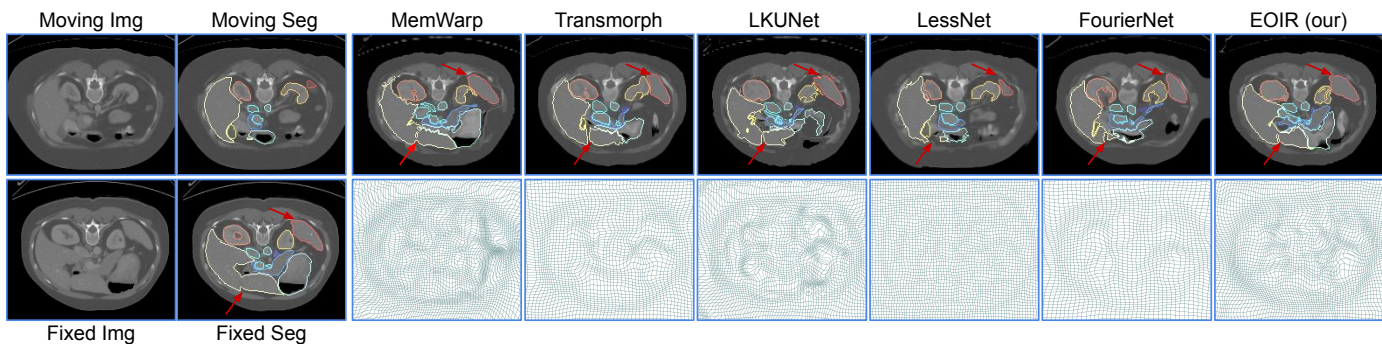


Fig. 7. Qualitative comparison on the abdomen CT dataset. TransMorph, LessNet, and FourierNet exhibit smooth deformation fields but fall short in anatomical alignment. MemWarp and LKUNet improve alignment but introduce more implausible voxels, while EOIR achieves a better accuracy-smoothness balance.

Table 3. Quantitative comparison on the OASIS dataset. Best-performing metrics are in bold. Symbols indicate direction:  $\uparrow$  for higher is better,  $\downarrow$  for lower is better. “Initial” refers to baseline results before registration. “TransMorph-1” and “TransMorph-2” denote versions with different smoothness regularization.

Model	Dice (%) $\uparrow$	HD95 (mm) $\downarrow$	SDlogJ $\downarrow$
Initial	57.18	3.83	-
VoxelMorph Balakrishnan et al. (2018)	84.70	1.55	0.13
TransMorph-1 Chen et al. (2022)	86.20	1.43	0.13
TransMorph-2 Chen et al. (2022)	88.54	1.27	0.50
LKUNet Jia et al. (2022)	88.61	<b>1.26</b>	0.52
LessNet Jia et al. (2024)	78.80	2.15	0.10
FourierNet Jia et al. (2023)	86.04	1.37	0.48
LapIRN Mok and Chung (2020b)	86.10	1.51	<b>0.07</b>
ConvexAdam Siebert et al. (2021)	84.64	1.50	<b>0.07</b>
EOIR ( $N_c=16$ )	86.96	1.38	0.28
<b>EOIR (Ours)</b>	<b>88.83</b>	1.28	0.52

Table 4. Quantitative comparison on the LUMIR dataset. Best-performing metrics are in bold. Symbols indicate direction:  $\uparrow$  for higher is better,  $\downarrow$  for lower is better. “Initial” refers to baseline results before registration. “EOIR (addition)” refers to using addition to compose deformation fields.

Model	Dice (%) $\uparrow$	HD95 (mm) $\downarrow$	NDV (%) $\downarrow$	TRE (mm) $\downarrow$
Initial	56.57	4.79	-	-
DeedsBCV Heinrich et al. (2013)	69.77	3.95	0.000	<b>2.22</b>
SynthMorph Hoffmann et al. (2021)	72.43	3.57	0.000	2.61
VoxelMorph Balakrishnan et al. (2018)	73.25	3.76	0.397	2.69
TransMorph Chen et al. (2022)	75.94	3.51	0.351	2.42
EOIR (addition)	77.34	3.34	0.186	2.37
<b>EOIR (Ours)</b>	<b>77.37</b>	<b>3.33</b>	<b>0.000</b>	2.35

#### 4.3.3. Handling Brain MR Image Registration

Unlike cardiac and abdomen datasets with different organ motions, inter-subject brain MR image registration requires fine-grained alignments of multiple variably shaped and sized brain structures. Table 3 presents the results of semi-supervised learning on the OASIS dataset. With similar field smoothness, EOIR outperforms both LKUNet and TransMorph-2 in Dice score. It is important to note that these models were trained semi-supervisedly, and the results are clearly influenced by the provided segmentation masks during training, as improvements in Dice score often correlate with less feasible deformation fields. The advantage of EOIR in this task primarily lies in the reduction of parameter size. With similar smoothness and a slightly higher Dice score, EOIR reduces network parameter size by 98.7% compared to TransMorph (71.59 MB) and by 97.3% compared to LKUNet (33.35 MB). Therefore, we further evaluate EOIR

on the LUMIR dataset, which is large-scale and trained in an unsupervised manner. As shown in Table 4, EOIR outperforms TransMorph by 1.9% with the NDV close to zero. Additionally, while SynthMorph Hoffmann et al. (2021) and DeedsBCV Heinrich et al. (2013) provide diffeomorphic deformation fields, their anatomical alignment falls short of EOIR. EOIR improves Dice by 6.8% and 10.9% respectively compared to SynthMorph and DeedsBCV.

#### 4.3.4. Handling Structures with Ambiguous Boundaries

The HippocampusMR dataset involves aligning two neighboring structures (the hippocampus head and body), with less defined boundaries compared to other anatomical regions. Quantitative results on this dataset are summarized in Table 5. Our EOIR framework consistently outperforms other approaches, except MemWarp Zhang et al. (2024a). MemWarp, designed for discontinuity-preserving registration, jointly predicts segmentation masks and deformation fields, enforcing stronger regularization on structural boundaries. While MemWarp achieves marginally higher Dice scores, its deformation fields are significantly less smooth than those produced by EOIR. This demonstrates EOIR’s superior balance between registration accuracy and deformation smoothness.

Table 5. Quantitative comparison on the HippocampusMR dataset. Best-performing metrics are in bold. Symbols indicate direction:  $\uparrow$  for higher is better,  $\downarrow$  for lower is better. “Initial” refers to baseline results before registration.

Model	Dice (%) $\uparrow$	HD95 (mm) $\downarrow$	SDlogJ $\downarrow$	Time $\downarrow$
Initial	62.46	12.39	-	-
VoxelMorph Balakrishnan et al. (2018)	80.97	7.90	0.06	0.19
TransMorph Chen et al. (2022)	84.90	6.19	0.07	0.49
RDP Wang et al. (2024)	86.13	6.02	0.07	0.46
CorrMLP Meng et al. (2024)	84.86	6.55	0.07	0.29
LessNet Jia et al. (2024)	75.59	9.28	0.05	0.30
FourierNet Jia et al. (2023)	80.10	7.59	0.06	0.33
LKUNet Jia et al. (2022)	75.09	9.29	0.04	0.39
MemWarp Zhang et al. (2024a)	<b>86.50</b>	<b>5.71</b>	0.24	0.96
<b>EOIR (Ours)</b>	86.44	6.20	0.10	0.35

#### 4.4. Results & Analysis on Computational Complexity

In this section, we provide results and analysis of EOIR regarding computational complexity. Two key parameters influence EOIR’s complexity: the number of convolutional layers  $n_c$  in

the encoder, and the start channel  $N_s$ , as depicted in Fig. 5. To provide a more striking comparison, we conduct complexity analysis using the most challenging abdomen dataset, alongside the ACDC dataset, which features much smaller image sizes compared to the other three datasets.

#### 4.4.1. Effects of $n_c$

As shown in Fig. 4, increasing  $n_c$  generally improves registration accuracy. However, starting from  $n_c = 3$ , the marginal benefits diminish rapidly with each additional layer. Interestingly, when replacing the encoder with a full U-Net, the accuracy decreases despite the increased parameter size. Sub-optimal methods like RDP and MemWarp, which utilize a similar U-Net architecture for pyramid registration, lag behind EOIR in all metrics. This suggests that mono-modal registration benefit more from local intensity linearization than from global bias harmonization, unlike affine registration Wang *et al.* (2023).

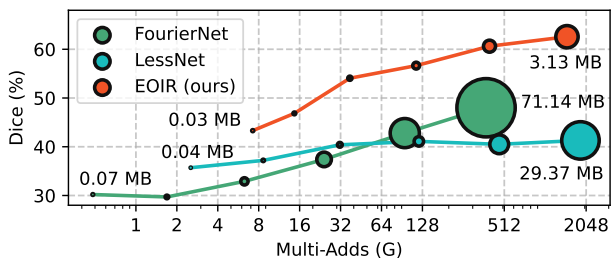


Fig. 8. Visual comparison of the trade-off between Dice and computational complexity for varying start channels ( $N_s$  from 2 to 64, doubling each step), compared to top-performing efficiency-driven methods on the Abdomen CT dataset. Circle size and label indicate network parameter size.

#### 4.4.2. Effects of $N_s$

Keeping three conv layers intact, we further study the impact of start channels  $N_s$  on the outcome. We compare EOIR with efficiency-driven methods, FourierNet and LessNet. As shown in Fig. 8, starting from  $N_s = 2$  for all methods, EOIR shows a much slower increase in parameter size compared to the other two. While both FourierNet and EOIR exhibit a log-linear increase in accuracy relative to multi-adds and parameter size, EOIR achieves a much better accuracy-efficiency balance than FourierNet. When assessed on the ACDC dataset, as shown in Table 2, EOIR’s improvement is more pronounced. EOIR ( $N_s = 8$ ) surpasses VoxelMorph, the runner-up in terms of complexity, with a significant increase in Dice score while maintaining lower multi-adds and parameter size. Also, EOIR ( $N_s = 8$ ) reduces the parameter size by 88.8% and multi-adds by 25.9% compared to RDP, the runner-up in accuracy, while achieving a slightly higher Dice score.

#### 4.4.3. Effects of Pyramid layers $n$

The number of pyramid layers  $n$  determines the ability of EOIR to capture large deformation. We plot the curve of the registration Dice with the increasing pyramid layers, as shown in Figure 9. For intra-patient registration on ACDC, three pyramid layers are sufficient to capture the ED-ES or ES-ED deformation. For inter-patient registration on abdomen images, the registration Dice keeps increasing from 1-5 pyramid layers. Therefore, to get

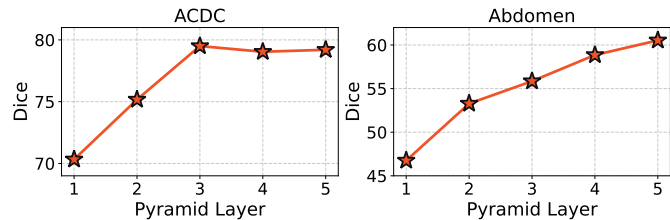


Fig. 9. Dice score with the increasing of pyramid layers in ACDC and Abdomen images.

the optimal number of pyramid layers, priors in the registration task should be considered, while a five-layer pyramid can work for most registration tasks.

#### 4.5. Results & Analysis on Smoothness & Diffeomorphism

In this section, we present the results and analysis of EOIR on deformation field smoothness. For the unsupervised setting, we evaluate the ACDC and LUMIR datasets, while for the semi-supervised setting, we focus on the Abdomen CT and OASIS datasets. We emphasize the use of Equation (7) for composing deformation fields across pyramid levels and time intervals. With  $n \times m$  sufficiently small time intervals, each deformation  $\phi^{ij}$  can be considered diffeomorphic. The composition is performed by resampling one deformation field by another, ensuring that the resulting deformation remains diffeomorphic, as described in Equation (7).

##### 4.5.1. Unsupervised

As shown in Table 2, all methods, except MemWarp (SDlogJ: 0.11), produced smooth outputs with SDlogJ values below 0.10. Notably, EOIR ( $N_s = 8$ ) achieves a lower SDlogJ while delivering a slightly better Dice score than the top-performing pyramid-based method, RDP, demonstrating EOIR’s superior handling of local motions during the cardiac cycle. In the brain MR registration, the effect of using the proposed composition method in Equation (7) becomes more evident. As seen in Table 4, additive composition results in significantly more non-diffeomorphic voxels for EOIR, whereas applying Equation (7) reduces NDV (%) to nearly zero without sacrificing accuracy (see Fig. 10 for a visual example). For other baseline methods, improvements in anatomical alignment are often accompanied by an increase in NDV (%).

##### 4.5.2. Semi-supervised

Semi-supervised learning often incorporates Dice loss to promote anatomical alignment, with the resulting deformation field typically being influenced by the segmentation masks. This can sometimes lead to implausible deformation fields, as the optimization is driven more by the mask alignment than the underlying image data. As shown in Table 3, methods including EOIR demonstrate that better anatomical alignment, indicated by higher Dice and lower HD95 (mm), often results in a larger SDlogJ, signaling a less smooth deformation field. For TransMorph, decreasing smoothness regularization leads to increasing Dice and decreasing SDlogJ. Similarly, for EOIR, by

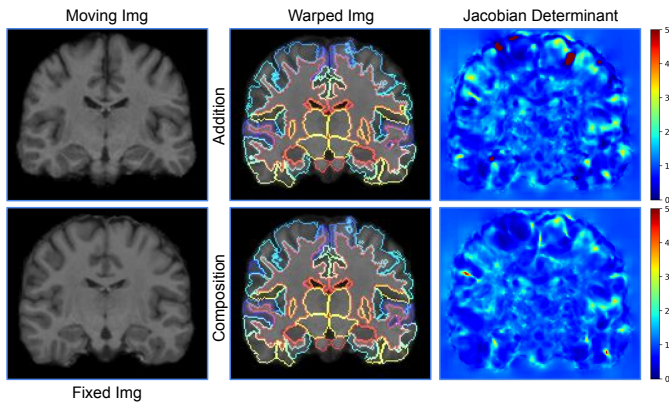


**Fig. 10.** Qualitative comparison between addition-based and composition-based registration in LUMIR. We present warped moving images and Jacobian determinants of deformation fields, with Jacobian determinant  $< 0$  highlighted in dark red.

simply reducing the start channel to  $N_s = 16$ , a similar accuracy-smoothness trade-off is observed. Abdomen CT dataset is more challenging as it has large deformation and limited training samples, and the accuracy-smoothness variations are larger than the OASIS. Therefore, we further study how smoothness regularization strength affect EOIR and other efficiency-driven methods. As shown in Fig. 11, for LessNet and FourierNet, decreasing  $\lambda$  reduces field smoothness while increasing Dice. However, EOIR, which employs Equation (7) for large-deformation diffeomorphic transformation, requires a more plausible field at each pyramid level to satisfy the assumptions. We found that decreasing  $\lambda$  initially increases Dice, peaking at  $\lambda = 1.0$ , before it declines. Additionally, varying  $n_c$  and  $N_s$  changes Dice, but SDlogJ remains around 0.17, highlighting the effectiveness of Equation (7) in handling large deformations (see Fig. 7).

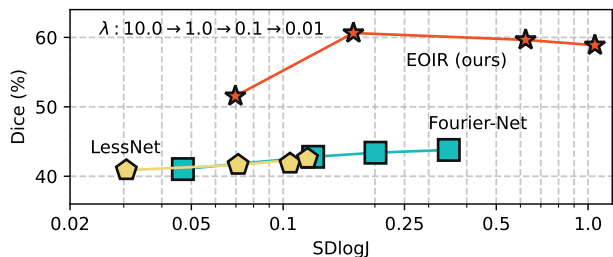


**Fig. 11.** Visual comparison of the trade-off between Dice and smoothness (SDlogJ) for varying  $\lambda$  in Equation (10) (0.1 to 10.0, increasing  $10\times$  per step), compared to efficiency-driven methods on the Abdomen CT dataset.

## 4.6. Discussion

### 4.6.1. Summary

Overall, EOIR achieves a superior balance between accuracy-efficiency and accuracy-smoothness in deformable image registration. Across five datasets with varying modalities and anatomies, EOIR reduces computational complexity without compromising accuracy. Moreover, the novel deformation field composition method in Equation (7) enables EOIR to maintain smoother deformation fields while preserving accuracy. The performance gains of EOIR stem from its integration of

the Horn–Schunck (H-S) assumption and the Linearization-Harmonization (L-H) assumption into the network design. We propose that a few convolutional layers are sufficient for feature extraction using a Laplacian feature pyramid, effectively linearizing local intensities and harmonizing mono-modal images at each pyramid level. The number of voxels satisfying the H-S assumption in both moving and fixed feature maps increases at each level, promoting displacement propagation within the smoothness regularization.

### 4.6.2. Advantages

Two major advantages emerge with the design of EOIR. **Expansibility:** EOIR’s simple architecture, consisting of just a few convolutional layers, makes it highly adaptable to incorporate advanced network modules such as large-kernel convolutions, transformer blocks, co-attention, and other novel structures. For instance, replacing the 3-layer ConvNet encoder with a full encoder-decoder U-net can enhance feature extraction capabilities. Additionally, incorporating larger-kernel convolutions or self-attention modules after the 3-layer ConvNet flow estimator can expand the network’s effective receptive field. **Economy:** EOIR’s efficient design significantly reduces computational complexity without sacrificing accuracy, making it well-suited for large volumetric images and deployment in resource-constrained settings. Specifically, Figure 8 illustrates the trade-off between Dice and computational complexity, measured by Multi-Adds (G) and network parameter size. Runtime comparisons among methods are shown in Table 2 and Table 5, demonstrating that all these learning-based methods can perform fast forward inference for volumetric registration within one second.

### 4.6.3. Zero-shot Inference Analysis

Beyond the results presented in this manuscript, the zero-shot inference capability of our EOIR framework has been further substantiated across multiple additional image registration tasks, as reported in Chen et al. (2025) (under the team name ‘next-gen-n’). Specifically, EOIR consistently ranks among the top three methods in registration accuracy for inter-subject registration using both the ADNI-1.5T and ADNI-3T datasets Lytle et al. (2020, 2021). It demonstrates particular strength in subject-to-atlas registration, achieving first place on the NIMH-T1w dataset Nugent et al. (2022) and second place on both the ADHD Lytle et al. (2020, 2021) and UltraCortex-9.4T Mahler et al. (2024) datasets. Across all these evaluations, EOIR achieves the lowest NDV among top-ranked approaches, underscoring its capacity to maintain diffeomorphic properties without compromising registration accuracy. Notably, EOIR is the only top-tier method that does not employ a progressive registration strategy, as highlighted in Chen et al. (2025). We posit that this advantage stems from the incorporation of the H–S and L–H assumptions into the network architecture, key elements overlooked by other methods. Their omission results in a less favorable balance between accuracy and computational efficiency, reinforcing EOIR’s value as an elegant and highly effective registration framework.

### 4.6.4. Broader Impact

Beyond benchmarking accuracy and efficiency, EOIR has broader implications for critical neuroimaging applications that

demand precise and stable voxel-to-voxel alignment. **Longitudinal image alignment:** Accurate deformable registration is fundamental for tracking intra-subject structural changes over time, such as lesion progression in multiple sclerosis (MS) or tumor evolution in oncology. By accurately aligning longitudinal images with smooth and efficient deformation fields that account for subject-specific brain atrophy, EOIR improves sensitivity to subtle lesion growth, shrinkage, or transformation, enabling reliable lesion- or tumor-level quantification across time points. This is exemplified in our recent work on longitudinal unique lesion tracking (AULTRA) (Zhang *et al.*, 2025c), which also leverages our advances in MS lesion segmentation (Zhang *et al.*, 2024c, 2025d) and filling (Zhang *et al.*, 2025e) as preprocessing for EOIR-based registration, followed by unique lesion identification (Rivas *et al.*, 2025) across time points. **Atlas construction:** Many population-level analyses, including those in quantitative susceptibility mapping (QSM) (Wang and Liu, 2015), rely on accurate voxel-wise correspondences across individuals. A future direction is to leverage EOIR for constructing susceptibility (Zhang *et al.*, 2018) and multimodal brain atlases with accurate voxel-wise alignment to study iron deposition, myelin integrity, and other quantitative biomarkers across the cohort.

#### 4.6.5. Limitations

EOIR has two main limitations. First, while EOIR achieves high accuracy and efficiency in mono-modal registration, its performance on multi-modal data is less effective. This occurs because the three-layer convolutional encoder, designed to linearize intensities and harmonize local contrast, lacks the capacity to learn cross-modal feature invariance Wang *et al.* (2023), which requires deeper networks to capture larger contextual regions. For example, when applied to the ThoraxCBCT dataset Hugo *et al.* (2017) (registering pre-therapeutic FBCT to low-dose CBCT), EOIR achieves a Dice score of 45%. Replacing the encoder with a full U-Net (while retaining the EOIR framework) increases Dice to 56%, validating the framework’s generalizability but highlighting the three-layer encoder’s trade-off between harmonization capacity and efficiency.

Second, EOIR shows diminished effectiveness when processing images that have fine-grained features, for example, lung nodules or retinal vessels. The reason lies in the feature pyramid design, which incorporates spatial downsampling. During this downsampling procedure, small structures like lung nodules or retinal vessels can be gradually reduced in prominence or even lost. As a result, at certain pyramid level  $i$ , the feature pyramid scheme is likely to miss objects with a largest diagonal dimension smaller than  $2^{(i-1)}$  voxels. Even if the displacement of these small objects may exceed their own size, this results in relatively poorer performance compared to cascaded methods.

## 5. Conclusion

In this paper, we introduced EOIR, a simple yet efficient image registration network that departs from conventional learning-based approaches by eliminating the decoder and relying solely on an encoder for feature extraction. This streamlined design substantially reduces the number of parameters compared to

traditional methods. Extensive experiments across four datasets demonstrate that EOIR not only achieves notable improvements in registration accuracy but also reduces network complexity, compared to state-of-the-art methods. EOIR effectively handles both small and large deformations through a novel deformation composition scheme, striking a balance between accuracy, efficiency, and smoothness. With lightweight design and strong performance, EOIR serves as a robust backbone for future developments in more complex registration architectures, offering a solid foundation for scaling in resource-constrained or large volumetric settings.

## References

- Arsigny, V., Commowick, O., Pennec, X., Ayache, N., 2006. A log-euclidean framework for statistics on diffeomorphisms, in: International Conference on Medical Image Computing and Computer-Assisted Intervention, Springer. pp. 924–931.
- Ashburner, J., 2007. A fast diffeomorphic image registration algorithm. *Neuroimage* 38, 95–113.
- Avants, B.B., Epstein, C.L., Grossman, M., Gee, J.C., 2008. Symmetric diffeomorphic image registration with cross-correlation: Evaluating automated labeling of elderly and neurodegenerative brain. *Medical Image Analysis* 12, 26–41.
- Balakrishnan, G., Zhao, A., Sabuncu, M.R., Guttag, J., Dalca, A.V., 2018. An unsupervised learning model for deformable medical image registration, in: Proceedings of the IEEE Conference on Computer Vision and Pattern Recognition, pp. 9252–9260.
- Balakrishnan, G., Zhao, A., Sabuncu, M.R., Guttag, J., Dalca, A.V., 2019. Voxelmorph: a learning framework for deformable medical image registration. *IEEE Transactions on Medical Imaging* 38, 1788–1800.
- Bernard, O., Lalonde, A., Zotti, C., Cervenansky, F., Yang, X., Heng, P.A., Cetin, I., Lekadir, K., Camara, O., Ballester, M.A.G., *et al.*, 2018. Deep Learning Techniques for Automatic MRI Cardiac Multi-structures Segmentation and Diagnosis: Is the Problem Solved? *IEEE Transactions on Medical Imaging* 37, 2514–2525.
- Chen, J., Frey, E.C., He, Y., Segars, W.P., Li, Y., Du, Y., 2022. Transmorph: Transformer for unsupervised medical image registration. *Medical Image Analysis* 82, 102615.
- Chen, J., Wei, S., Honkamaa, J., Martinen, P., Zhang, H., Liu, M., Zhou, Y., Tan, Z., Wang, Z., Wang, Y., *et al.*, 2025. Beyond the lumir challenge: The pathway to foundational registration models. *arXiv preprint arXiv:2505.24160*.
- Chen, M., Carass, A., Reich, D.S., Calabresi, P.A., Pham, D., Prince, J.L., 2013. Voxel-wise displacement as independent features in classification of multiple sclerosis, in: Proceedings of SPIE, pp. 10–1117.
- Chen, X., Diaz-Pinto, A., Ravikumar, N., Frangi, A.F., 2021a. Deep learning in medical image registration. *Progress in Biomedical Engineering* 3, 012003.
- Chen, X., Liu, M., Wang, R., Hu, R., Liu, D., Li, G., Zhang, H., 2024. Spatially covariant image registration with text prompts. *IEEE Transactions on Neural Networks and Learning Systems*, 1–11.
- Chen, X., Xia, Y., Ravikumar, N., Frangi, A.F., 2021b. A deep discontinuity-preserving image registration network, in: International Conference on Medical Image Computing and Computer Assisted Intervention, Springer. pp. 46–55.
- Dalca, A.V., Balakrishnan, G., Guttag, J., Sabuncu, M.R., 2018. Unsupervised learning for fast probabilistic diffeomorphic registration, in: International Conference on Medical Image Computing and Computer Assisted Intervention, Springer. pp. 729–738.
- Dalca, A.V., Balakrishnan, G., Guttag, J., Sabuncu, M.R., 2019. Unsupervised Learning of Probabilistic Diffeomorphic Registration for Images and Surfaces. *Medical Image Analysis* 57, 226–236.
- Ding, X., Zhang, X., Han, J., Ding, G., 2022. Scaling up your kernels to 31x31: Revisiting large kernel design in cnns, in: Proceedings of the IEEE/CVF Conference on Computer Vision and Pattern Recognition, pp. 11963–11975.
- Dosovitskiy, A., Beyer, L., Kolesnikov, A., Weissenborn, D., Zhai, X., Unterthiner, T., Dehghani, M., Minderer, M., Heigold, G., Gelly, S., *et al.*, . An image is worth 16x16 words: Transformers for image recognition at scale, in: International Conference on Learning Representations.

- Dufumier, B., Grigis, A., Victor, J., Ambrose, C., Frouin, V., Duchesnay, E., 2022. Openbb: a large-scale multi-site brain mri data-set for age prediction and debiasing. *NeuroImage* 263, 119637.
- Fechter, T., Baltas, D., 2020. One-shot learning for deformable medical image registration and periodic motion tracking. *IEEE Transactions on Medical Imaging* 39, 2506–2517.
- Ghahremani, M., Khateri, M., Jian, B., Wiestler, B., Adeli, E., Wachinger, C., 2024. H-vit: A hierarchical vision transformer for deformable image registration, in: *Proceedings of the IEEE/CVF Conference on Computer Vision and Pattern Recognition*, pp. 11513–11523.
- Heinrich, M.P., Jenkinson, M., Brady, M., Schnabel, J.A., 2013. Mrf-based deformable registration and ventilation estimation of lung ct. *IEEE Transactions on Medical Imaging* 32, 1239–1248.
- Hering, A., Hansen, L., Mok, T.C., Chung, A.C., Siebert, H., Häger, S., Lange, A., Kuckertz, S., Heldmann, S., Shao, W., et al., 2022. Learn2reg: comprehensive multi-task medical image registration challenge, dataset and evaluation in the era of deep learning. *IEEE Transactions on Medical Imaging* 42, 697–712.
- Hoffmann, M., Billot, B., Greve, D.N., Iglesias, J.E., Fischl, B., Dalca, A.V., 2021. Synthmorph: learning contrast-invariant registration without acquired images. *IEEE Transactions on Medical Imaging* 41, 543–558.
- Hoopes, A., Hoffmann, M., Fischl, B., Gutttag, J., Dalca, A.V., 2021. Hypermorph: Amortized hyperparameter learning for image registration, in: *International Conference on Information Processing in Medical Imaging*, Springer. pp. 3–17.
- Horn, B.K., Schunck, B.G., 1981. Determining optical flow. *Artificial Intelligence* 17, 185–203.
- Hu, X., Wang, Y., Fuxin, L., Samaras, D., Chen, C., 2021. Topology-aware segmentation using discrete morse theory, in: *International Conference on Learning Representations*. URL: <https://openreview.net/forum?id=LGgdb4TS4Z>.
- Hugo, G.D., Weiss, E., Sleeman, W.C., Balik, S., Keall, P.J., Lu, J., Williamson, J.F., 2017. A longitudinal four-dimensional computed tomography and cone beam computed tomography dataset for image-guided radiation therapy research in lung cancer. *Medical physics* 44, 762–771.
- Islam, M.A., Jia, S., Bruce, N.D., 2020a. How much position information do convolutional neural networks encode?, in: *International Conference on Learning Representations*.
- Islam, M.A., Jia, S., Bruce, N.D., 2020b. How much position information do convolutional neural networks encode? *arXiv preprint arXiv:2001.08248*.
- Jia, X., Bartlett, J., Chen, W., Song, S., Zhang, T., Cheng, X., Lu, W., Qiu, Z., Duan, J., 2023. Fourier-net: Fast image registration with band-limited deformation, in: *Proceedings of the AAAI Conference on Artificial Intelligence*, pp. 1015–1023.
- Jia, X., Bartlett, J., Zhang, T., Lu, W., Qiu, Z., Duan, J., 2022. U-net vs transformer: Is u-net outdated in medical image registration?, in: *International Workshop on Machine Learning in Medical Imaging*, Springer. pp. 151–160.
- Jia, X., Lu, W., Cheng, X., Duan, J., 2024. Decoder-only image registration. *arXiv preprint arXiv:2402.03585*.
- Jia, X., Thorley, A., Chen, W., Qiu, H., Shen, L., Styles, I.B., Chang, H.J., Leonardi, A., De Marvao, A., O'Regan, D.P., et al., 2021. Learning a model-driven variational network for deformable image registration. *IEEE Transactions on Medical Imaging* 41, 199–212.
- Kang, M., Hu, X., Huang, W., Scott, M.R., Reyes, M., 2022. Dual-stream pyramid registration network. *Medical Image Analysis* 78, 102379.
- Kervadec, H., Bouchtiba, J., Desrosiers, C., Granger, E., Dolz, J., Ayed, I.B., 2019. Boundary loss for highly unbalanced segmentation, in: *International Conference on Medical Imaging with Deep Learning*, PMLR. pp. 285–296.
- Lee, C.Y., Xie, S., Gallagher, P., Zhang, Z., Tu, Z., 2015. Deeply-supervised nets, in: *Artificial Intelligence and Statistics*, Pmlr. pp. 562–570.
- Li, Z., Tian, L., Mok, T.C., Bai, X., Wang, P., Ge, J., Zhou, J., Lu, L., Ye, X., Yan, K., et al., 2023. Samconvx: Fast discrete optimization for ct registration using self-supervised anatomical embedding and correlation pyramid, in: *International Conference on Medical Image Computing and Computer-Assisted Intervention*, Springer. pp. 559–569.
- Liu, Y., Chen, J., Wei, S., Carass, A., Prince, J., 2024. On finite difference jacobian computation in deformable image registration. *International Journal of Computer Vision* , 1–11.
- Liu, Z., Lin, Y., Cao, Y., Hu, H., Wei, Y., Zhang, Z., Lin, S., Guo, B., 2021. Swin transformer: Hierarchical vision transformer using shifted windows, in: *Proceedings of the IEEE/CVF International Conference on Computer Vision*, pp. 10012–10022.
- Luo, W., Li, Y., Urtasun, R., Zemel, R., 2016. Understanding the effective receptive field in deep convolutional neural networks. *Advances in Neural Information Processing Systems* 29.
- Lytle, M.N., Burman, D.D., Booth, J.R., 2021. A neuroimaging dataset on response inhibition and selective attention in adults and children with and without adhd. *Data in Brief* 37, 107158.
- Lytle, M.N., Hammer, R., Booth, J.R., 2020. A neuroimaging dataset on working memory and reward processing in children with and without adhd. *Data in Brief* 31, 105801.
- Ma, T., Zhang, S., Li, J., Wen, Y., 2024. Iirp-net: Iterative inference residual pyramid network for enhanced image registration, in: *Proceedings of the IEEE/CVF Conference on Computer Vision and Pattern Recognition*, pp. 11546–11555.
- Mahler, L., Steiglechner, J., Bender, B., Lindig, T., Ramadan, D., Bause, J., Birk, F., Heule, R., Charyasz, E., Erb, M., et al., 2024. Ultracortex: Submillimeter ultra-high field 9.4 t brain mr image collection and manual cortical segmentations. *arXiv preprint arXiv:2406.18571*.
- Marcus, D.S., Wang, T.H., Parker, J., Csernansky, J.G., Morris, J.C., Buckner, R.L., 2007. Open access series of imaging studies (oasis): cross-sectional mri data in young, middle aged, nondemented, and demented older adults. *Journal of Cognitive Neuroscience* 19, 1498–1507.
- Meng, M., Bi, L., Fulham, M., Feng, D., Kim, J., 2023. Non-iterative coarse-to-fine transformer networks for joint affine and deformable image registration, in: *International Conference on Medical Image Computing and Computer-Assisted Intervention*, Springer. pp. 750–760.
- Meng, M., Feng, D., Bi, L., Kim, J., 2024. Correlation-aware coarse-to-fine mlps for deformable medical image registration, in: *Proceedings of the IEEE/CVF Conference on Computer Vision and Pattern Recognition*, pp. 9645–9654.
- Mok, T.C., Chung, A., 2020a. Fast symmetric diffeomorphic image registration with convolutional neural networks, in: *Proceedings of the IEEE/CVF Conference on Computer Vision and Pattern Recognition*, pp. 4644–4653.
- Mok, T.C., Chung, A.C., 2020b. Large deformation diffeomorphic image registration with laplacian pyramid networks, in: *International Conference on Medical Image Computing and Computer Assisted Intervention*, Springer. pp. 211–221.
- Mok, T.C., Chung, A.C., 2021. Large deformation image registration with anatomy-aware laplacian pyramid networks, in: *Segmentation, Classification, and Registration of Multi-modality Medical Imaging Data: MICCAI 2020 Challenges*, Springer. pp. 61–67.
- Nugent, A.C., Thomas, A.G., Mahoney, M., Gibbons, A., Smith, J.T., Charles, A.J., Shaw, J.S., Stout, J.D., Namyst, A.M., Basavaraj, A., et al., 2022. The nimh intramural healthy volunteer dataset: A comprehensive meg, mri, and behavioral resource. *Scientific Data* 9, 518.
- Pratt, W.K., Kane, J., Andrews, H.C., 1969. Hadamard transform image coding. *Proceedings of the IEEE* 57, 58–68.
- Rivas, C.A., Zhang, J., Wei, S., Remedios, S.W., Carass, A., Prince, J.L., 2025. Unique ms lesion identification from mri, in: *Medical Imaging 2025: Image Processing*, SPIE. pp. 592–599.
- Ronneberger, O., Fischer, P., Brox, T., 2015. U-net: Convolutional networks for biomedical image segmentation, in: *International Conference on Medical Image Computing and Computer-Assisted Intervention*, Springer. pp. 234–241.
- Sandler, M., Howard, A., Zhu, M., Zhmoginov, A., Chen, L.C., 2018. Mobilenetv2: Inverted residuals and linear bottlenecks, in: *Proceedings of the IEEE Conference on Computer Vision and Pattern Recognition*, pp. 4510–4520.
- Shi, J., He, Y., Kong, Y., Coatrieux, J.L., Shu, H., Yang, G., Li, S., 2022. Xmorpher: Full transformer for deformable medical image registration via cross attention, in: *International Conference on Medical Image Computing and Computer-Assisted Intervention*, Springer. pp. 217–226.
- Siebert, H., Hansen, L., Heinrich, M.P., 2021. Fast 3d registration with accurate optimisation and little learning for learn2reg 2021, in: *International Conference on Medical Image Computing and Computer-Assisted Intervention*, Springer. pp. 174–179.
- Simpson, A.L., Antonelli, M., Bakas, S., Bilello, M., Farahani, K., Van Ginneken, B., Kopp-Schneider, A., Landman, B.A., Litjens, G., Menze, B., et al., 2019. A large annotated medical image dataset for the development and evaluation of segmentation algorithms. *arXiv preprint arXiv:1902.09063*.
- Su, L.M., Vagvolgyi, B.P., Agarwal, R., Reiley, C.E., Taylor, R.H., Hager, G.D., 2009. Augmented reality during robot-assisted laparoscopic partial nephrectomy: toward real-time 3d-ct to stereoscopic video registration. *Urology* 73, 896–900.

- Taha, A., Gilmore, G., Abbass, M., Kai, J., Kuehn, T., Demarco, J., Gupta, G., Zajner, C., Cao, D., Chevalier, R., et al., 2023. Magnetic resonance imaging datasets with anatomical fiducials for quality control and registration. *Scientific Data* 10, 449.
- Ulyanov, D., 2016. Instance normalization: The missing ingredient for fast stylization. *arXiv preprint arXiv:1607.08022*.
- Vercateren, T., Pennec, X., Perchant, A., Ayache, N., 2009. Diffeomorphic demons: Efficient non-parametric image registration. *NeuroImage* 45, S61–S72.
- Wang, A.Q., Evan, M.Y., Dalca, A.V., Sabuncu, M.R., 2023. A robust and interpretable deep learning framework for multi-modal registration via keypoints. *Medical Image Analysis* 90, 102962.
- Wang, H., Ni, D., Wang, Y., 2024. Recursive deformable pyramid network for unsupervised medical image registration. *IEEE Transactions on Medical Imaging*, 1–1 doi:10.1109/TMI.2024.3362968.
- Wang, J., Zhang, M., 2020. Deepflash: An efficient network for learning-based medical image registration, in: *Proceedings of the IEEE/CVF Conference on Computer Vision and Pattern Recognition*, pp. 4444–4452.
- Wang, Y., Liu, T., 2015. Quantitative susceptibility mapping (qsm): decoding mri data for a tissue magnetic biomarker. *Magnetic resonance in medicine* 73, 82–101.
- Xu, Z., Lee, C.P., Heinrich, M.P., Modat, M., Rueckert, D., Ourselin, S., Abramson, R.G., Landman, B.A., 2016. Evaluation of six registration methods for the human abdomen on clinically acquired ct. *IEEE Transactions on Biomedical Engineering* 63, 1563–1572.
- Yang, L., Li, W., Shu, Y., Mi, J., Huang, Y., Xiao, B., 2024. Shiftmorph: A fast and robust convolutional neural network for 3d deformable medical image registration, in: *ACM Multimedia*.
- Zhang, H., Chen, X., Hu, R., Liu, D., Li, G., Wang, R., 2024a. Memwarp: Discontinuity-preserving cardiac registration with memorized anatomical filters, in: *International Conference on Medical Image Computing and Computer-Assisted Intervention*, Springer. pp. 671–681.
- Zhang, H., Chen, X., Wang, R., Hu, R., Liu, D., Li, G., 2024b. Slicer networks. *arXiv preprint arXiv:2401.09833*.
- Zhang, H., Hu, R., Chen, X., Liu, M., Wang, Y., Wang, R., Zhang, J., Li, G., Cheng, X., Duan, J., 2025a. Unsupervised deformable image registration with structural nonparametric smoothing, in: *International Conference on Information Processing in Medical Imaging*, Springer. pp. 108–124.
- Zhang, H., Wang, R., Zhang, J., Liu, D., Li, C., Li, J., 2023. Spatially covariant lesion segmentation, in: *Proceedings of the Thirty-Second International Joint Conference on Artificial Intelligence*, pp. 1713–1721.
- Zhang, H., Zhang, Y., Wang, J., Chen, X., Hu, R., Tian, X., Li, G., Liu, M., 2025b. Voxelopt: Voxel-adaptive message passing for discrete optimization in deformable abdominal ct registration. *arXiv preprint arXiv:2506.19975*.
- Zhang, J., Rivas, C., Dewey, B.E., Wei, S., Zhang, H., Remedios, S.W., Hays, S.P., Wang, S., Zuo, L., Mowry, E.M., Newsome, S.D., Saidha, S., Calabresi, P.A., Prince, J.L., Carass, A., 2025c. Automated unique lesion tracking (aultra): A framework for longitudinal lesion-wise morphometry analysis in multiple sclerosis, in: *Radiological Society of North America (RSNA) Annual Meeting, Chicago, IL, USA. Abstract, Poster Presentation*.
- Zhang, J., Zuo, L., Dewey, B.E., Remedios, S.W., Liu, Y., Hays, S.P., Pham, D.L., Mowry, E.M., Newsome, S.D., Calabresi, P.A., et al., 2025d. Uniself: A unified network with instance normalization and self-ensembled lesion fusion for multiple sclerosis lesion segmentation. *arXiv preprint arXiv:2508.03982*.
- Zhang, J., Zuo, L., Dewey, B.E., Remedios, S.W., Pham, D.L., Carass, A., Prince, J.L., 2024c. Towards an accurate and generalizable multiple sclerosis lesion segmentation model using self-ensembled lesion fusion, in: *2024 IEEE International Symposium on Biomedical Imaging (ISBI)*, IEEE. pp. 1–5.
- Zhang, J., Zuo, L., Liu, Y., Remedios, S., Landman, B.A., Prince, J.L., Carass, A., 2025e. Bi-directional ms lesion filling and synthesis using denoising diffusion implicit model-based lesion repainting, in: *Medical Imaging 2025: Image Processing*, SPIE. pp. 217–223.
- Zhang, Y., Wei, H., Cronin, M.J., He, N., Yan, F., Liu, C., 2018. Longitudinal atlas for normative human brain development and aging over the lifespan using quantitative susceptibility mapping. *Neuroimage* 171, 176–189.
- Zhao, S., Dong, Y., Chang, E.I., Xu, Y., et al., 2019a. Recursive cascaded networks for unsupervised medical image registration, in: *Proceedings of the IEEE/CVF International Conference on Computer Vision*, pp. 10600–10610.
- Zhao, S., Lau, T., Luo, J., Chang, E.I., Xu, Y., 2019b. Unsupervised 3d end-to-end medical image registration with volume tweening network. *IEEE Journal of Biomedical and Health Informatics* doi:10.1109/JBHI.2019.2951024.

## 6. Appendix

### 6.1. Heatmap Generation of Fig. 1

As part of our methodology for crafting the heatmap depicted in Fig. 1 of the main text, we began by training the EOIR network, with start channels  $N_s = 32$ , on the abdomen CT dataset. Subsequently, we randomly selected an image from this dataset as the fixed image and derived the moving image by translating it one voxel anteriorly.

With the new moving and fixed images as inputs, we used the 3-layer encoder to extract a 32-channel feature map. To make the output visually interpretable, we applied Principal Component Analysis (PCA) to reduce the channels to one, retaining only the component with the largest variance. The heatmap was computed using the formula  $(\mathbf{I}_m(p) - \mathbf{I}_f(p)) / \frac{\partial \mathbf{I}_f}{\partial y}(p)$ . Post-processing involved thresholding, where invalid voxels were set to 0 and valid voxels to 1. A 2D heatmap was then generated by averaging all slices along the axis direction and visualized using the ‘viridis’ color map to enhance clarity and interpretation. The untrained heatmap was generated following the same process as described above, but with the encoder initialized randomly.

### 6.2. Training Details for Each Dataset

During training, all networks were trained for 300 epochs on the abdominal, LUMIR, and ACDC datasets, except for the OASIS dataset, which required an extended training period of 700 epochs for optimal performance. For the abdominal and OASIS datasets, we employed NCC loss and Dice loss for similarity (with  $NCC : Dice : regularization = 1 : 1 : 1$ ). In contrast, for the ACDC dataset, MSE loss was used for training, where  $\lambda = 0.01$  was set to achieve the best registration performance. To train our EOIR on the LUMIR dataset, NCC was applied as the similarity loss, with  $\lambda = 5$  and a learning rate of  $4e^{-4}$ .

### 6.3. Ablation Study on the Encoder Design

A detailed analysis of how the number of convolution layers  $n_c$  in encoder affects registration performance is presented in Table 6. ‘EOIR-1CONV’ to ‘EOIR-6CONV’ represent models with  $1 \sim 6$   $3 \times 3 \times 3$  convolution layers in the encoder. ‘EOIR-0CONV’ uses an untrainable  $1 \times 1 \times 1$  convolution to expand the input channel dimension to match the start channel size, effectively functioning like no convolution, as it barely affect local details. ‘EOIR-UNet’ applies a traditional UNet in the encoder. The registration Dice improves with up to three convolution layers, but adding more than three yields diminishing returns. Using a UNet increases model complexity significantly, yet results in lower accuracy. Thus, three convolution layers strike an optimal balance between registration accuracy and model complexity.

### 6.4. Boxplot Results in ACDC Dataset and Abdomen Image Dataset

The boxplot results in Figure 12 and Figure 14 present the per-organ Dice and Avg. Dice scores of EOIR and the comparator methods. We compared EOIR against four top-performing methods: MemWarp, FourierNet, LKUNet, and RDP. In cardiac image registration, EOIR achieved a significantly higher Avg. Dice score than all other methods ( $p < 0.05$ , t-test on

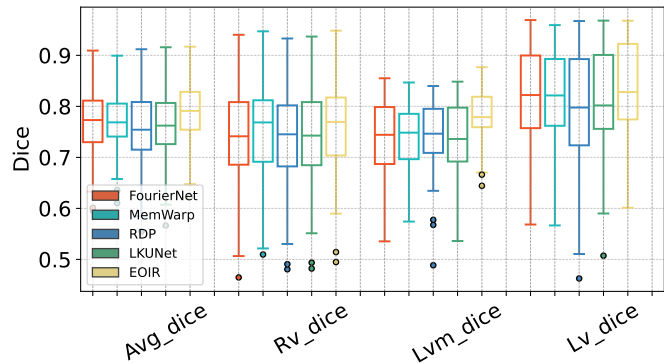


Fig. 12. Boxplot results on cardiac MR image registration, where we compare our EOIR with MemWarp, FourierNet, LKUNet and RDP.

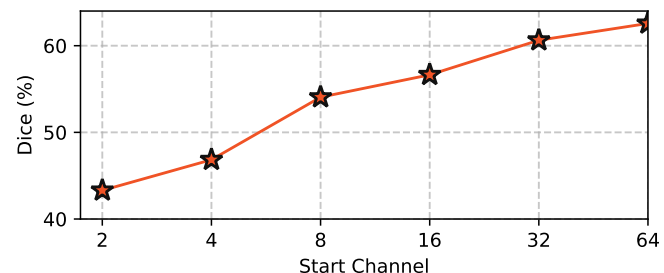


Fig. 13. Dice scores of EOIR with the increasing start channels  $N_s$  on abdomen image registration.

Dice score). Similarly, in abdominal image registration, EOIR outperformed the other methods in Avg. Dice score ( $p < 0.05$ ), except for RDP ( $p = 0.099$ ).

### 6.5. Effects of Varying Start Channels

We investigate the impact of varying the number of start channels  $N_s$  on registration performance. As shown in Figure 13, Dice scores increase with  $N_s$  initially but plateau after  $N_s = 32$ , accompanied by an exponential rise in model parameters. Thus, we set  $N_s = 32$  for most experiments in this work.

### 6.6. LUMIR Ranking on Test Phase

In the test phase of the LUMIR challenge, we still won the second ranking, with the detailed top three results in Table 7. It can be observed that our EOIR achieves similar registration accuracy while keeping a significantly smoother deformation field, compared to the rest approaches.

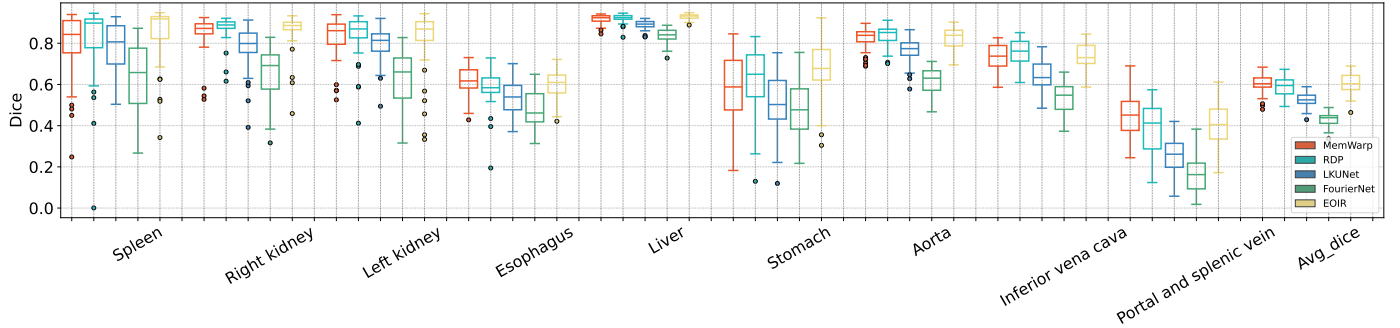


Fig. 14. Boxplot results on abdominal image registration, where we compare our EOIR with MemWarp, FourierNet, LKUNet and RDP.

Table 6. Quantitative comparison of registration results on the abdominal CT dataset, featuring different variations of EOIR. Metrics including Dice (%), HD95 (mm), SDlogJ, multi-adds and Params are averaged across all image pairs for each method. Symbols indicate the desired direction of metric values:  $\uparrow$  implies higher is better, while  $\downarrow$  indicates lower is better. “Initial” refers to the baseline results before registration.

Model	Dice (%) $\uparrow$	HD95 (mm) $\downarrow$	SDlogJ $\downarrow$	Multi-Adds (GB) $\downarrow$	Params (MB) $\downarrow$
Initial	30.86	29.77	-	-	-
EOIR-0CONV	43.39	27.85	0.170	179.35	0.80
EOIR-1CONV	54.40	21.26	0.172	180.98	0.80
EOIR-2CONV	55.92	20.92	0.177	235.40	0.83
EOIR-3CONV	60.64	17.61	0.173	398.60	0.91
EOIR-4CONV	61.54	18.15	0.172	616.16	1.02
EOIR-5CONV	62.23	17.17	0.170	833.72	1.13
EOIR-6CONV	62.58	17.23	0.170	1050.00	1.24
EOIR-UNet	58.27	17.22	0.168	1300.00	15.25

Table 7. Quantitative results on the LUMIR dataset test phase, comparing EOIR with baseline methods and other participating teams.

Team	TRE_LM $\downarrow$	DSC (%) $\uparrow$	HD95 (mm) $\downarrow$	NDV $\downarrow$	Rank Score $\uparrow$	Rank $\uparrow$
Initial	4.38	0.55	4.91	-	-	-
honkamj	3.09	0.79	3.04	0.0025	0.814	1
<b>hnuzyx_next-gen-nn (ours)</b>	3.12	0.78	3.28	0.0001	0.781	2
lieuweaver	3.07	0.78	3.29	0.0121	0.737	3
uniGradICONwIO50	3.14	0.76	3.40	0.0002	0.668	7
VFA	3.14	0.78	3.15	0.0704	0.667	8
TransMorph	3.14	0.76	3.46	0.3621	0.518	11
deedsBCV	3.10	0.70	3.94	0.0002	0.423	13
uniGradICON	3.24	0.74	3.57	0.0001	0.402	14
SynthMorph	3.23	0.72	3.61	0.0000	0.361	17
ANTsSyN	3.48	0.70	3.69	0.0000	0.265	19
VoxelMorph	3.53	0.71	4.07	1.2167	0.157	20